Toward High-Performance Wrist-Worn Energy Harvester via Hybrid Approach

Mingjing Cai , *Member, IEEE*, and Wei-Hsin Liao , *Senior Member, IEEE*

Abstract—We propose a hybrid approach to enhance the power generation performance of wrist-worn energy harvester. Based on a highly compact framework, the energy harvester integrates a planetary gear system to increase energy conversion capacity, an asymmetric carrier to improve motion capacity, and a magnetic spring to enhance displacement and velocity responses. These power enhancement mechanisms work together to boost the output power of the energy harvester. We develop an analytical model to theoretically investigate the effects of different power enhancement mechanisms. A miniature prototype with a total volume of 2.01 cm^3 is fabricated and tested under bench-top excitations. The experiments include air gap determination of the magnetic spring and measurement of output power for various power enhancement configurations. It is found that the planetary gear system improves the power of conventional wrist-worn energy harvester by 335%–1422%. Based on this, the asymmetric carrier and magnetic spring can further increase the power by 35%–373% and 16%–278%, respectively. If hybridizing the power enhancement mechanisms, the output power can reach 8–28 times that of the conventional structure and the maximum power achieves 326.27±17.46 μW at 1.2 Hz.

Index Terms—Arm swing, electromagnetic transducer, energy harvesting, hybrid approach, wearable.

I. INTRODUCTION

ENERGY harvesting from human motion for powering wearables has attracted significant attention in recent years [1], [2]. This technology provides a promising solution to address some issues of conventional batteries in various applications, such as Internet of Things (IoTs) applications [3], [4], [5]. Constrained by finite energy capacity, conventional batteries are incapable of meeting the need for long-term and continuous sensing in IoT applications [6], [7]. In addition, conventional batteries seem to be less environmentally friendly since the life of numerous electronics is prematurely terminated by battery deterioration after years' usage. Instead, the biomechanical energy of human motion is considered as a sustainable and green energy source, which enables energy harvesting technology to realize self-powered IoT applications. Among reported biomechanical energy harvesters [8], wrist-worn energy harvesters have the advantages of good wearability and wide excitation range. For instance, a woodpecker mimic structure integrated into the watchband was developed to scavenge the kinetic energy of human arm swinging [9]. Furthermore, wrist-worn energy harvesters can be embedded in the wearables to improve application feasibility and user experience [10]. However, a major obstacle to embedding the energy harvesters in wearables is the need for supplying a significant amount of electrical energy when embedded in a limited space. To take up this challenge, great efforts have been put to improve the performance of wrist-worn energy harvesters from different perspectives. Generally speaking, wrist-worn energy harvesters utilize an eccentric weight to capture the kinetic energy of human arm swing motion and then use a transducer to convert the captured energy into electricity [11]. In this manner, the power enhancement methods can be categorized into three types: increase the eccentric weight to improve captured kinetic energy (motion capture capacity) without enlarging the volume; employ special mechanisms to enhance the displacement and velocity responses via potential energy manipulation; and exploit special mechanisms or designs to improve energy conversion capacity of the transducer by increasing the transducer's operating frequency. Although these approaches are realized with the help of special mechanisms, the power improvement can outweigh the additional space occupation of these mechanisms and improve the power density of the energy harvester.

For the first power enhancement approach, a straightforward way is to use a large proof mass, but it would make the energy harvester bulky. A more cost-effective approach takes advantage of the asymmetric structure, which has intrinsic eccentric weight to serve as the proof mass without increasing the total volume of the energy harvester [12]. For example, Liu et al. [13] employed an asymmetric magnet to serve as proof mass and the rotor of the electromagnetic transducer. A similar idea was also reported by Maharjan et al. [14] who used a magnetic ball to excite a hybridized electromagnetic-triboelectric transducer, and it produced a maximum power of 94 μW. More recently, Cai and Liao [15] used the transducer to act as the

This article has been accepted for inclusion in a future issue of this journal. Content is final as presented, with the exception of pagination.

2   IEEE/ASME TRANSACTIONS ON MECHATRONICS

proof mass such that no additional eccentric weight was needed, which generated a maximum power of 1.46 mW. These devices usually replaced the proof mass with asymmetric designs of the transducers. However, these asymmetric designs give rise to an issue that the transducers cannot efficiently convert the captured energy. As for enhancing displacement and velocity responses, springs are introduced to change the system potential energy, thereby increasing the response displacement and velocity under the same excitation [16]. Halim et al. [17] applied a torsional spring to a wrist-worn energy harvester that has vertically upward proof mass to enhance the displacement and velocity responses and power output (maximum power of 61 μW). Cai and Liao [18] exploited the negative stiffness of a repulsive magnetic spring to effectively improve the power generation performance of wrist-worn energy harvester (maximum power of 151 μW). Other than these approaches, it is an alternative solution to enhance power output by increasing the energy conversion capacity of the transducer. For this purpose, frequency-up conversion mechanisms are invited to boost the frequency of captured motion, which equivalently increases the energy conversion capacity of the transducer. Therefore, the plucking mechanism is explored to overcome low-frequency human motion excitation [19], [20]. This mechanism uses "catch to release" effect of the cantilever beam such that the transducer can work at a natural frequency of the beam regardless of the excitation frequency. The transducers with the plucking mechanism, however, are incapable of continuously converting energy and thus the generated energy is constrained. Another frequency-up conversion approach is to adopt the spur gear train, which proportionally accelerates the captured motion and thus improves the energy conversion capacity of wrist-worn energy harvester. The first attempt at using a spur gear system was made by Seiko Automatic Generation System (maximum power of 50 μW) [21]. Later, Kinetron Inc. launched its microgenerator system (MGS) (maximum power of 97 μW) that utilizes a similar spur gear train as the frequency-up converter [22]. Other than the mechanical gear system, Cai et al. [23], [24] explored a radial magnetic frequency-up converter to increase the energy conversion capacity and compactness of wrist-worn energy harvester (maximum power of 1.74 mW). Zhou et al. [25] also developed an improved wrist-worn energy harvester using an axial magnetic frequency-up converter. These works have laid a solid foundation for enhancing the power generation of wrist-worn energy harvesters from different perspectives. However, they only focused on one of the power enhancement approaches and some of them seem to be incompatible with the others because of structural constraints, physical constraints, and electromechanical coupling interface. Furthermore, as every power enhancement mechanism should require extra space, it is challenging to apply multiple power enhancement mechanisms in a highly confined space of wrist-worn energy harvesters. Given these issues, it raises a question: is it possible to hybridize various kinds of power enhancement approaches within a highly confined space to pursue the synergy effect of these approaches? To answer this question, it is worth exploring a hybrid approach with low cost of the device space to integrate multiple power enhancement mechanisms such that they can work together to further boost the performance. In addition, it is of interest and benefit to provide an in-depth analysis and comparison of different approaches under the same framework.

In this article, we propose to integrate multiple power enhancement approaches into a highly compact wrist-worn energy harvester. The proposed energy harvester employs a planetary gear system as the frequency-up converter to increase energy conversion capacity, a tiny magnetic spring to enhance displacement and velocity responses, as well as an asymmetric structure of the planetary gear system to improve motion capture capacity. Meanwhile, these mechanisms are integrated into a compact framework, which enables the energy harvester to achieve high power output and power density. Based on this structure, the energy harvester is modeled to analyze the effects of different power enhancement mechanisms. A miniature prototype is also fabricated to experimentally determine the air gap of the magnetic spring and to compare the performances of different power enhancement mechanisms.

This rest of this article is organized as follows. Section II will describe the structure and principles of the proposed energy harvester. A comprehensive model of the energy harvester will be derived in Section III. Section IV will present experimental results and discussions. Finally, Section V concludes this article.

II. PRINCIPLES AND DESIGN OF ENERGY HARVESTER

In this section, the framework of the energy harvester will be first introduced. Based on this framework, the power enhancement mechanisms that are integrated into the energy harvester will be illustrated.

A. Framework of Energy Harvester

As mentioned, the wrist-worn energy harvester usually contains a rotational proof mass and a transducer. To improve the power and power density, a rotational electromagnetic transducer is adopted because of its high energy conversion efficiency and geometry compatibility with the proof mass [26]. In this manner, the proof mass and the rotor of the transducer can share the same axis of rotation. Starting from this fundamental structure of wrist-worn energy harvester, a planetary gear system is selected as the frequency-up converter since its input and output motions are coaxial. Therefore, the proof mass, frequency-up converter, and transducer can be coaxially arranged to improve structure compactness. As shown in Fig. 1, the framework of the energy harvester comprises a motion capture unit (proof mass), a frequency-up converter (planetary gear system), and a power generation unit (electromagnetic transducer). This framework provides a compact structure for the energy harvester that allows it to be embedded in a wrist-worn wearable electronic. Note that the planetary gear structure of this framework already enables the frequency-up conversion feature of the energy harvester. When the human arm swings, the motion is captured by the proof mass and accelerated by the frequency-up converter. Excited by high-frequency motion, the transducer efficiently converts kinetic energy into electrical energy.
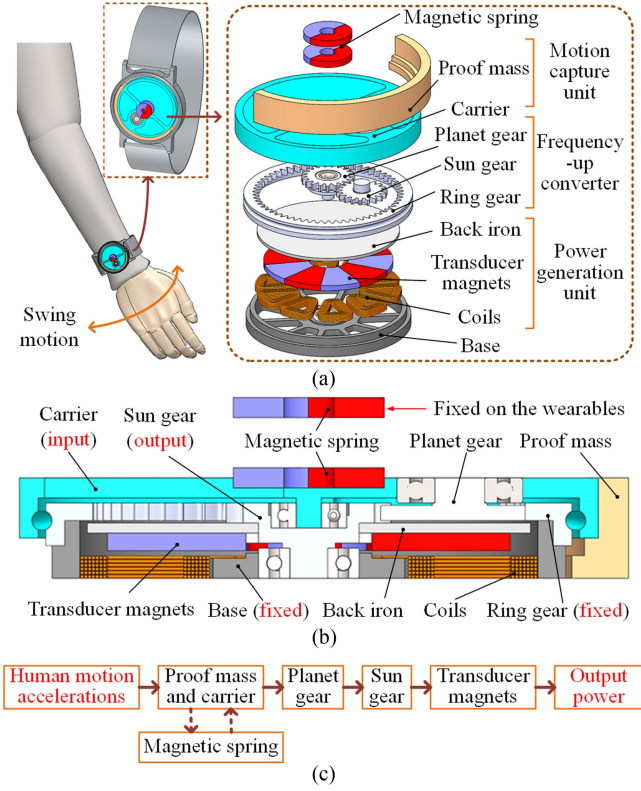
Fig. 1. Framework architecture of the energy harvester. (a) Exploded view of the energy harvester. (b) Cross-sectional view of the energy harvester. (c) Motion transmission diagram for the system. The motion transmitted to the magnetic spring is only applicable when it is activated.
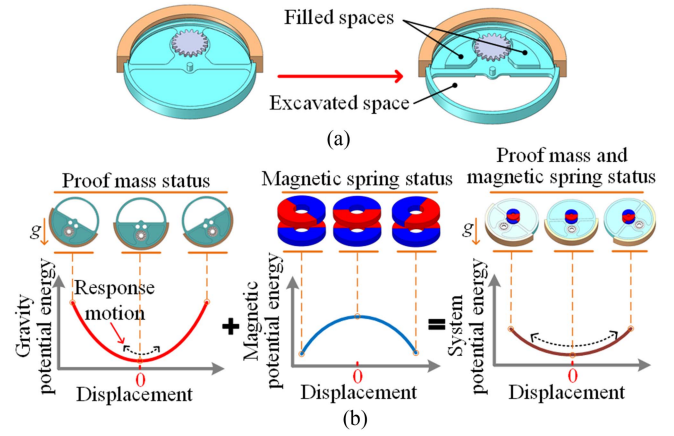

Fig. 2. Principles of the power enhancement mechanisms. (a) Asymmetric carrier. Half of the carrier is excavated while the other half is filled with materials without interfering with the motion of the planetary gear system. (b) Principles of repulsive magnetic spring. The symbol "g" denotes the direction of gravity acceleration and the zero points at each horizontal axis represent the stable equilibrium points of the proof mass.

TABLE I
PARAMETERS OF THE ENERGY HARVESTER

Symbol	Parameter	Value
N_p	Number of pole pairs of magnet array	1 for the spring's magnets
		5 for the transducer
B_r	Remanence of the magnets	1.25 T for the spring
		1.45 T for the transducer
N_c	Total number of coils	10
R_i	Internal resistance	117 Ω
T_1	Teeth numbers of the sun gear	20
T_2	Teeth numbers of the planet gear	20
T_3	Teeth numbers of the ring gear	60

B. Principles of Hybrid Performance Enhancement Approach

The framework enables the energy harvester to be equipped with a hybrid power enhancement approach. Thanks to the motion amplification effect of the planetary gear system, the energy conversion capacity of the transducer can be significantly improved. Based on this framework, motion capture capacity improvement is realized by exploiting an asymmetric design of the carrier, as shown in Fig. 2(a). The carrier is installed on the ring gear via a ball bearing that only allows rotational motion of the carrier. A half of the carrier adjacent to the proof mass is filled with the base material while the other half is excavated to create additional eccentric mass for the energy harvester. As a result, the carrier also belongs to the motion capture unit. Since the motion capture capacity is positively correlated with the eccentric mass, the asymmetric design of the carrier enables the energy harvester to gain additional eccentric mass without paying the price of extra space. Different from the previous works [13], [14], [15], the asymmetric carrier of this energy harvester does not compromise the energy conversion capacity of the transducer for two reasons: it is incorporated into the frequency-up converter, instead of the transducer. In this manner, the coils and the magnets of the transducer can be fully utilized since they can simultaneously participate in energy conversion; it does not affect the transmission ratio of the frequency-up converter because the space of the gears is not occupied by the additional material.

The last power enhancement approach integrated into the energy harvester is introducing a tiny repulsive magnetic spring. As shown in Fig. 1(b), a pair of permanent magnets is mounted on the carrier to rotate in relation to the base while the other one is fixed. These two pairs of permanent magnets are reversely polarized such that repulsive torque is exerted on the carrier when the proof mass oscillates around its stable equilibrium point. Fig. 2(b) schematically depicts the potential energy with respect to displacement of the proof mass with and without the magnetic spring. It is shown that the magnetic spring adds symmetric negative stiffness to the energy harvesting system, which effectively lowers the system potential energy well depth. Under the same excitation, the proof mass obtains larger displacement and velocity to enhance power generation. This approach employs magnetic interaction to enhance the displacement and velocity responses of the energy harvester without increasing mechanical friction. Furthermore, since the magnetic spring only takes away around 2.3% of the energy harvester's volume and part of it is embedded into the carrier, the additional space for the magnetic spring is negligible. Key design parameters of the energy harvester are given in Table I.
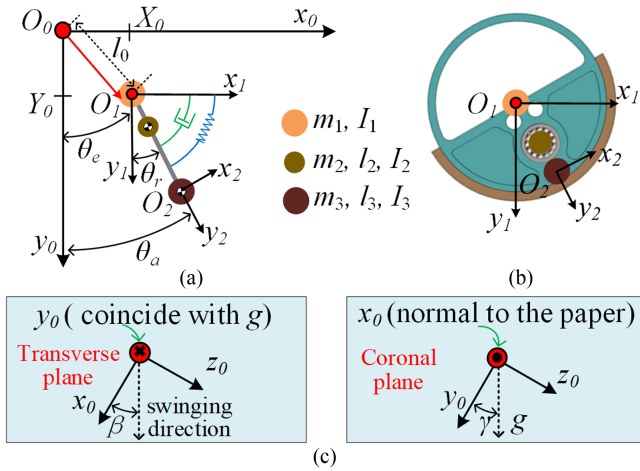
Fig. 3. Lumped model for energy harvesting system dynamics. (a) Schematic model for system dynamics of the energy harvesting system on the sagittal plane. (b) Corresponding coordinate frames and masses. (c) Illustration of the out-of-plane angles β and γ.

Note that empirical values of the gears are selected considering the tradeoff between gear ratio and mechanical friction, space limitation, and manufacturing difficulty.

Compared with the fundamental structure of wrist-worn energy harvester (only comprising a proof mass and a transducer), the planetary gear system of this energy harvester occupies around one-third of the total volume to increase energy conversion capacity. However, benefiting from the framework of the energy harvester, the other power enhancement methods can be integrated into the planetary gear system with minimal space. Thus, integrating multiple approaches with minimal space becomes an advantage over the competitors. In the following sections, it will be theoretically and experimentally shown that the power improvement will significantly outweigh the additional volume that is used for integrating the hybrid power enhancement approach.

III. SYSTEM MODEL OF ENERGY HARVESTER

In this section, a mathematical model of the energy harvesting system will be derived to analyze the performances of different power enhancement mechanisms.

A. System Dynamics

A schematic model of the proposed energy harvesting system is shown in Fig. 3. In this lumped model, the energy harvesting system consists of a damper, a nonlinear spring, and three masses. The damper represents system energy dissipation caused by mechanical friction and electricity generation, while the nonlinear spring results from the repulsive magnetic spring. The masses account for the movable components of the energy harvester: m_1 is the combined mass of the sun gear, the permanent magnets, the back iron, the rotor, and I_1 is the moment of inertia about its center of mass (COM); m_2 is the mass of the planet gear, and I_2 is the moment of inertia about their COM. The distance l_2 denotes the center distance between the

planet gear and the sun gear; and m_3 is the combined mass of the carrier and proof mass and it has eccentric length l_3 and moment of inertia I_3 about its COM. Note that the planetary gear system amplifies the rotational velocity of the proof mass. The transmission ratios of the sun gear and planet gear to the proof mass are calculated as $i_s = T_3/T_1 + 1$ and $i_p = -(T_3/T_2 + 1)$, respectively. Here, T_1, T_2, and T_3 are the teeth numbers of the sun gear, planet gear, and ring gear, respectively. In this derivation, all the vectors are highlighted in bold to avoid confusion. For simplification, it is assumed that only the arm swing motion on the sagittal plane is considered as the excitation of the energy harvester, and the out-of-plane rotation is ignored. Lagrangian approach is used to derive the equation of motion and multiple coordinate frames are introduced: coordinate O_0 is the inertial reference frame; coordinate O_1 denotes the reference frame that is fixed at the center of the base; and coordinate O_2 is fixed on the COM of mass m_3. To consider a general model for arbitrary excitations on the sagittal plane, an accelerometer is assumed to be secured on coordinate O_1 to collect excitation accelerations. Since an accelerometer typically reports the sum of excitation acceleration plus gravity acceleration, the potential energy contributed by gravity is ignored in the Lagrangian, and the gravity is treated as part of the excitation accelerations [15]. The acquired human motion accelerations $\ddot{X}_1$, $\ddot{Y}_1$, and $\ddot{\theta}_e$ serve as input of the dynamic model. Based on these, the system kinetic energy can be obtained as

$$T = \frac{1}{2} \left\{ I_1 \left(i_s \dot{\theta}_r \right)^2 + I_2 \left(i_p \dot{\theta}_r + \dot{\theta}_a \right)^2 + I_3 \dot{\theta}_a^2 + \sum_{j=1}^{3} m_j \|\boldsymbol{v}_j\|^2 \right\} \tag{1}$$

where $\boldsymbol{v}_j$ denotes the translational velocities of masses m_2 and m_3 and their subscript index is consistent with these masses. The angular speeds $\dot{\theta}_r$ and $\dot{\theta}_a$ are defined in Fig. 3. The sum of the first three terms represents the rotational component of system kinetic energy while the last one is the translational component. The vector form of the translational velocities can be expressed in coordinate O_1

$$\boldsymbol{v}_j = \begin{bmatrix} \dot{X}_1 \cos\theta_e + \dot{Y}_1 \sin\theta_e + l_j \dot{\theta}_a \cos\theta_a \\ -\dot{X}_1 \sin\theta_e + \dot{Y}_1 \cos\theta_e - l_j \dot{\theta}_a \sin\theta_a \end{bmatrix}, j = 1, 2, 3 \tag{2}$$

where l_1 denotes the eccentric length from its center and thus it equals zero. In the energy harvesting system, the captured kinetic energy is dissipated via mechanical friction and the transducer. Rayleigh dissipation function is employed to account for the damping effect

$$R = b\dot{\theta}_r^2 / 2 \tag{3}$$

where b is the combined damping coefficient of mechanical friction and energy conversion. If there is no magnetic spring, the equation of motion can be derived as

$$\ddot{\theta}_r = -\left\{ (\alpha m_2 + m_3) l_3 \left[\ddot{X}_1 \cos\theta_r - \ddot{Y}_1 \sin\theta_r \right] \right.$$
$$\left. + b\dot{\theta}_r + I_e \ddot{\theta}_e \right\} / I_c \tag{4}$$

This article has been accepted for inclusion in a future issue of this journal. Content is final as presented, with the exception of pagination.

CAI AND LIAO: TOWARD HIGH-PERFORMANCE WRIST-WORN ENERGY HARVESTER VIA HYBRID APPROACH 5

where $I_c = m_2 l_2^2 + m_3 l_3^2 + I_3 + (i_p + 1)^2 I_2 + i_s^2 I_1$ and $I_e = m_2 l_2^2 + m_3 l_3^2 + I_3 + (i_p + 1) I_2$. So far, the system dynamics model is applicable to the sagittal plane. With different orientations of the device, there exist nonzero out-of-plane angles β (on the transverse plane) and γ (on the coronal plane), as shown in Fig. 3(c). To account for the effects of β and γ, the excitation accelerations $\ddot{X}_1$ and $\ddot{Y}_1$ can be expressed as

$$\begin{bmatrix} \ddot{X}_1 \\ \ddot{Y}_1 \end{bmatrix} = \begin{bmatrix} \ddot{X}_{1e} \\ \ddot{Y}_{1e} \end{bmatrix} \cos\beta - \begin{bmatrix} -g\sin\theta_e \\ g\cos\theta_e \end{bmatrix} \cos\gamma \qquad (5)$$

where $\ddot{X}_{1e}$ and $\ddot{Y}_{1e}$ (expressed in framework O_1) are the accelerations solely excited by human arm swinging. The model can be extended to different orientations of the device by substituting (5) into (4). The magnetic spring adds a symmetric nonlinear repulsive torque that is the function of θ_1 to the proof mass. Thus, the equation of motion becomes (6) shown at the bottom of this page.

The magnetic torque T_z of the spring represents the interaction between the proof mass and the magnetic spring. It will be analytically derived to solve the equation of motion. The mechanical and electrical domains of the system are coupled by the coefficient b. With the states of the relative angle between coordinate O_1 and coordinate O_2, an analytical model will be constructed to calculate the generated power.

B. Magnetic Spring Model

The magnet sectors of the magnetic spring and the transducer are axially magnetized, and the adjacent magnet sectors have alternating polarities. Given this, a general model can be derived to describe the magnetic field distributions of the magnetic spring and the transducer. Except for the permanent magnets and back iron, the other components are made of nonferromagnetic materials whose magnetic permeability is approximately equal to that of the air. Therefore, they are ignored in this model. The existence of the back iron affects the magnetic field distribution of the magnetic spring and the transducer. However, the back iron significantly shields the magnetic field excited by the transducer magnets such that the magnetic interference (MI) between the magnetic spring and the transducer is negligible.
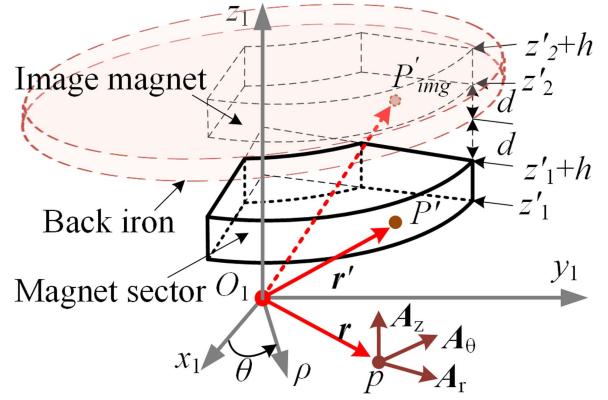

Fig. 4. Schematic model of the magnet array. Note that only one magnet sector of the magnet array is shown.

Thus, their magnetic field distribution can be independently modeled. Considering an axially magnetized magnet array with alternating polarities of adjacent poles and an infinitely large back iron, as shown in Fig. 4, the magnetic field at a point P outside the magnets can be regarded as the superposition of the magnet array and its image magnets. The mirror image method would not cause significant errors in magnetic field distribution if the back iron is sufficiently large. For clarification, the prime symbol is used to indicate the coordinates of the image and real magnets, while the coordinates of the point P are represented without prime symbols. The radial and tangential components of the magnetic potential vector at a point outside the magnets can be given as

In (7) and (8) shown at the bottom of this page, B_r, N_p, and h are the remanence of the magnets, pole number of the magnet array, and thickness of the magnet sector, respectively. In addition, $k = 1$ and 2 denote the cases for real magnets and image magnets, respectively. The integral limits $r'_{j,k,1}$, $r'_{j,k,2}$, $\theta'_{j,k,1}$ and $\theta'_{j,k,2}$ are the inner radius, outer radius, left-side angle, and right-side angle of the jth real or image magnet sector, respectively. The integral limit $z'_{j,k}$ satisfies that $z'_{j,2} - z'_{j,1} = 2d + h$. Here, d is the air gap between the magnet array and the back iron, and it

$$\ddot{\theta}_r = -\left\{ (\alpha m_2 + m_3) l_3 \left[\left(\ddot{X}_{1e} \cos\theta_r - \ddot{Y}_{1e} \sin\theta_r \right) \cos\beta + g\sin\theta_a \cos\gamma \right] + b\dot{\theta}_r - T_z(\theta_r) + I_e \ddot{\theta}_e \right\} \Big/ I_c \qquad (6)$$

$$A_r(\boldsymbol{r}) = \frac{B_r}{4\pi} \sum_{j=1}^{N_P} \sum_{i=1}^{2} \sum_{k=1}^{2} (-1)^{j+i+1}$$

$$\left[\int_{z'_{j,k}}^{z'_{j,k}+h} \int_{\theta'_{j,k,1}}^{\theta'_{j,k,2}} \frac{\sin(\theta-\theta')}{|\boldsymbol{r}-\boldsymbol{r}'|} \bigg|_{r'_j = r'_{j,k,i}} r'_{j,k,i} d\theta' dz' - \int_{z'_{j,k}}^{z'_{j,k}+h} \int_{r'_{j,k,1}}^{r'_{j,k,2}} \frac{\cos(\theta-\theta')}{|\boldsymbol{r}-\boldsymbol{r}'|} \bigg|_{\theta'_j = \theta'_{j,k,i}} dr' dz' \right] \qquad (7)$$

$$A_\theta(\boldsymbol{r}) = \frac{B_r}{4\pi} \sum_{j=1}^{N_P} \sum_{i=1}^{2} \sum_{k=1}^{2} (-1)^{j+i+1}$$

$$\left[\int_{z'_{j,k}}^{z'_{j,k}+h} \int_{\theta'_{j,k,1}}^{\theta'_{j,k,2}} \frac{\cos(\theta-\theta')}{|\boldsymbol{r}-\boldsymbol{r}'|} \bigg|_{r'_j = r'_{j,k,i}} r'_{j,k,i} d\theta' dz' + \int_{z'_{j,k}}^{z'_{j,k}+h} \int_{r'_{j,k,1}}^{r'_{j,k,2}} \frac{\sin(\theta-\theta')}{|\boldsymbol{r}-\boldsymbol{r}'|} \bigg|_{\theta'_j = \theta'_{j,k,i}} dr' dz' \right]. \qquad (8)$$

This article has been accepted for inclusion in a future issue of this journal. Content is final as presented, with the exception of pagination.

6   IEEE/ASME TRANSACTIONS ON MECHATRONICS

equals zero for the transducer since the back iron is attached to the magnet array.

With the radial and tangential components of the magnetic potential vector, the axial component of the magnetic flux density at point P is written as

$$B_z(r) = \frac{1}{r}\left[\frac{\partial}{\partial r}rA_\theta(r) - \frac{\partial}{\partial \theta}A_r(r)\right]. \tag{9}$$

So far, (7) and (9) provide a general model to calculate the radial and tangential components of the magnetic potential vector and the axial component of the magnetic flux density at point P. Based on this model, we can further derive the magnetic torque of the magnetic spring and the generated power of the transducer. For the magnetic spring, after obtaining the magnetic field distribution of the magnets that are mounted on the carrier, the equivalent surface current of the other pair of magnets can be calculated via $j_M = M \times n$ (M and n are the magnetization intensity of the magnets and normal unit vector, respectively). Then the magnetic torque can be given as

$$T_z = \int_s \boldsymbol{\rho} \times [\boldsymbol{j_M} \times B_z(r)]\,dS$$

$$= \sum_{i=1}^{N_p}(-1)^{i+1}2M\int_{z_1}^{z_2}\int_{r_1}^{r_2}rB_z(r)|_{\theta=\theta_i}drdz. \tag{10}$$

Here, z_1, z_2, r_1, r_2, θ_1, and θ_2 are the upper surface height, lower surface height, inner radius, outer radius, left-side angle, and right-side angle of the magnets that are fixed. Note that the coordinates of these magnets are not denoted with prime symbols since they are used to describe the geometry of the equivalent surface current. From the derived model, the magnetic torque implicitly depends on the air gap between two pairs of magnets and their relative displacement $\theta_r = \theta'_1 - \theta_1$.

C. Power Generation Model

The transducer contains a set of coils in series. Each coil comprises a set of stacked layers of copper wires, and each layer consists of concentric copper sectors. Given the relative angle between coordinate O_1 and coordinate O_2, the magnetic flux linkage of the copper coils can be obtained by integrating the magnetic potential vector alone the copper coils, which is expressed as

$$\varphi(\theta_r)$$

$$= N_c\sum_{n=1}^{N}\left(\int_{r_{n,1}}^{r_{n,2}}A_r(r)|_{\theta=\theta_{n,1}}dr + \int_{r_{n,2}}^{r_{n,1}}A_r(r)|_{\theta=\theta_{n,2}}dr\right.$$

$$+\left.\int_{\theta_{n,1}}^{\theta_{n,2}}A_\theta(r)r|_{r=r_{n,2}}d\theta + \int_{\theta_{n,2}}^{\theta_{n,1}}A_\theta(r)r|_{r=r_{n,1}}d\theta\right) \tag{11}$$

where N_c and N are the number of the coils and the turns number of a coil, respectively. Then, the derivative of the magnetic flux linkage with respect to time gives the induced electromagnetic force of the transducer

$$E(t) = -\frac{d\varphi(\theta_r)}{dt} = -\frac{d\varphi(\theta_r)}{d\theta_r}\dot{\theta}_r. \tag{12}$$

Since the excitation frequency of human motion is around 1 Hz, the inductance of the coils is negligibly small and can be ignored. Then the circuit model of the energy harvester can be described as a voltage source and a series internal resistance. Assume a resistor is connected across the terminals of the coils, the average output power can be calculated

$$P_{avr} = \frac{1}{T}\int_t^{t+T}i_L(t)^2R_L dt$$

$$= \frac{1}{T}\int_t^{t+T}E(t)^2R_L\Big/(R_i + R_L)^2dt. \tag{13}$$

Here, i_L, R_i, and R_L are the load current, internal, and load resistances, respectively. T denotes the time of a walking cycle. If the load resistance is equal to the internal resistance, the optimal output power can be achieved. The fully coupled system model can be summarized as state space form (14) shown at the bottom of this page where $x_1 = \theta_r$ and $x_2 = \dot{\theta}_r$. The output power $y(t)$ is the output of the energy harvesting system, which is consistent with the diagram shown in Fig. 1(c). On the basis of average power, the optimal load resistance, which may not be equal to the internal resistance, should depend on the excitation frequency and amplitude for a given device. However, a load resistor that is equal to the internal resistance can guarantee that the least electrical energy is wasted on the coils and will provide a great convenience for theoretical and experimental analysis.

So far, it is ready to evaluate the average output power using the above equations and the excitation accelerations $\ddot{X}_1$ and $\ddot{Y}_1$ as input. Since it is difficult to obtain the analytical solution to (6), one can numerically solve it with the help of MATLAB. Using the expression of the magnetic torque T_z, (6) can be numerically solved by MATLAB ODE tools, and the states of θ_r are acquired. Substituting states of θ_r into (12) and (13) yields the average output power.

D. Simulation of Energy Harvesting System

As discussed, the magnetic field distribution is analytically modeled based on the assumptions of infinitely large back iron

$$\begin{bmatrix}\dot{x}_1\\\dot{x}_2\end{bmatrix} = \begin{bmatrix}x_2\\(-bx_2 + T_z)/I_c\end{bmatrix} + \begin{bmatrix}0\\\left\{-(\alpha m_2 + m_3)l_3\left[\left(\ddot{X}_{1e}\cos x_1 - \ddot{Y}_{1e}\sin x_1\right)\cos\beta + g\sin\theta_a\cos\gamma\right] - I_e\ddot{\theta}_e\right\}/I_c\end{bmatrix}$$

$$y(t) = (d\varphi/dx_1)^2x_2^2R_L\Big/(R_i + R_L)^2 \tag{14}$$

This article has been accepted for inclusion in a future issue of this journal. Content is final as presented, with the exception of pagination.

CAI AND LIAO: TOWARD HIGH-PERFORMANCE WRIST-WORN ENERGY HARVESTER VIA HYBRID APPROACH 7
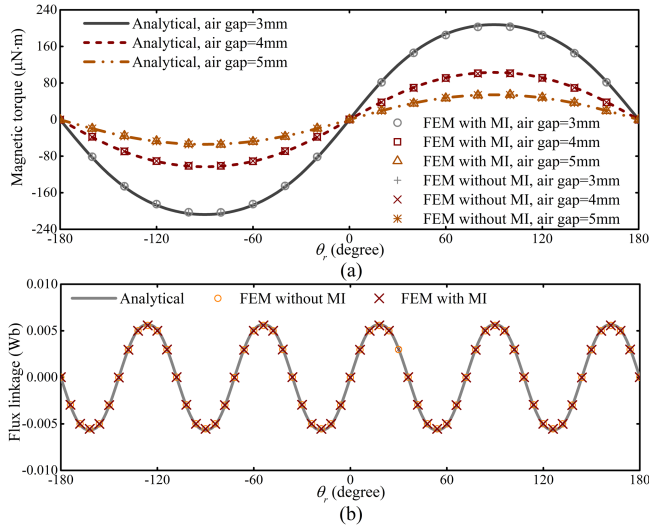
Fig. 5. Magnetic torque and flux linkage of the coils for various air gaps between the magnets of the magnetic spring. (a) Magnetic torque with respect to θ_r for analytical model and FEM. (b) Flux linkage with respect to θ_r for analytical model and FEM. The air gap of the magnetic spring in FEM is 3 mm. The FEM results with and without MI are almost overlapped.

TABLE II
CONFIGURATIONS OF POWER ENHANCEMENT MECHANISMS

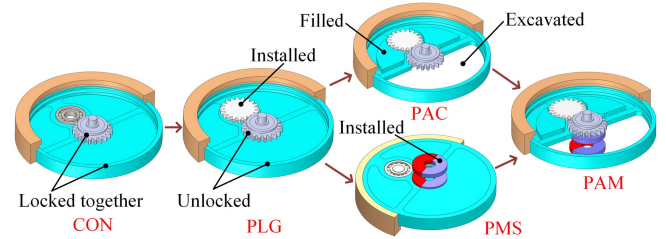| Configuration	Active approach(es)
CON	N.A.
PLG	Planetary gear system
PAC	Planetary gear system and asymmetric carrier
PMS	Planetary gear system and magnetic spring
PAM	Planetary gear system, asymmetric carrier, and magnetic spring

Fig. 6. Components modification for different configurations. The planetary gear system is installed on the backside of PMS.

and MI cancellation. To verify the analytical model, the finite-element model (FEM) is performed using ANSYS Electromagnetic Suite (ANSYS Inc., USA). In the analysis, the parameters of the permanent magnets and the back iron are consistent with the designed ones. The magnetic torque of the magnetic spring and flux linkage of the coils with and without MI are calculated via FEM. To this end, both permanent magnets of the transducer and the magnetic spring are modeled in the FEM to consider MI while the irrelevant magnets are removed to obtain the results without MI.

The magnetic torque and flux linkage generated by the analytical model and FEM are shown in Fig. 5. It is found that there are no significant differences between the FEM results with and without MI, which implies that the magnetic spring and the transducer can be independently modeled. This is attributed to the careful design of the magnets' number of pole pairs. In addition, the analytical torque of the magnetic spring and the flux linkage of the transducer match well with the FEM results, which verifies the analytical model of the magnetic spring. Although the analytical model is expected to slightly overestimate the result, it seems that the differences between the analytical model and FEM are barely sensible since the designed back iron is sufficiently large. Therefore, the analytical model would not cause significant error in predicting the power output of the energy harvester and it has significant advantages in computation speed and optimization. It can also be found from Fig. 5(b) that the magnetic force is positive when $\theta_r > 0$ and it becomes negative if $\theta_r < 0$. This indicates that the magnetic spring creates a negative stiffness in the system.

Based on the analytical model and the designed parameters of the energy harvester, simulations are performed to predict the effects of different power enhancement mechanisms. For this purpose, different combinations of power enhancement mechanisms are configured to evaluate their effects. As given in Table II, conventional structure (CON) only has the architecture of a conventional wrist-worn energy harvester and serves as the control group to quantify the power improvement brought by different approaches. In this configuration, the carrier is locked with the sun gear. Compared with CON configuration, planetary gear system structure (PLG) equips the planetary gear system, but the asymmetric carrier and magnetic spring are disabled. Based on PLG configuration, planetary gear system and asymmetric carrier structure (PAC) and planetary gear system and magnetic spring structure (PMS) enable asymmetric carrier and magnetic spring, respectively. For PAM configuration, all three approaches are activated in the energy harvester. The components modification for different configurations are shown in Fig. 6. To mimic the motion of human arm swinging, a swinging pendulum with harmonic motion is assumed to excite the energy harvester in the simulation. The parameters of different configurations are given in Table III. The configurations satisfy the models constructed in Section III, but the parameters m_3, I_3, l_3, and damping coefficient vary for different configurations. The damping coefficients of different configurations are experimentally determined, and the experiment details will be illustrated in Section IV. Apart from these parameters, special treatment is required for some configurations when they are simulated with a unified system dynamics model. First, the magnetic torque T_z is set to zero for the configurations without the magnetic spring, such as CON, PLG, and PAC. Then the transmission ratio i_s equals zero for CON.

The average power of PMS and PAM configurations with respect to the air gap of the magnetic spring is shown in Fig. 7. It is found that with a decreased air gap, the average power generally increases and reaches the peak. This is attributed to increasing repulsive magnetic torque that helps the proof mass escape from the stable equilibrium point. However, if the air gap continues to decrease, the power plunges to the valley point

TABLE III
PARAMETERS OF DIFFERENT CONFIGURATIONS

Symbol	Parameter	Value*
I_1	Moment of inertia of the sun gear, the permanent magnets, the back iron and the rotor	4.67×10^{-8} kg·m²
m_2	Eccentric mass of the planet gear	0.33 g
I_2	Moment of inertia of the planet gear	3.09×10^{-9} kg·m²
l_2	Center distance between the planet gear and the sun gear	6 mm
m_3	Eccentric mass of the carrier and proof mass	6.04 g for CON 6.04 g for PLG 6.83 g for PAC 6.04 g for PMS 6.83 g for PAM
I_3	Moment of inertia of the carrier and proof mass	5.58×10^{-7} kg·m² for CON 5.58×10^{-7} kg·m² for PLG 5.09×10^{-7} kg·m² for PAC 5.58×10^{-7} kg·m² for PMS 5.09×10^{-7} kg·m² for PAM
l_3	Eccentric length of the carrier and proof mass	4.01 mm for CON 4.01 mm for PLG 5.99 mm for PAC 4.01 mm for PMS 5.99 mm for PAM

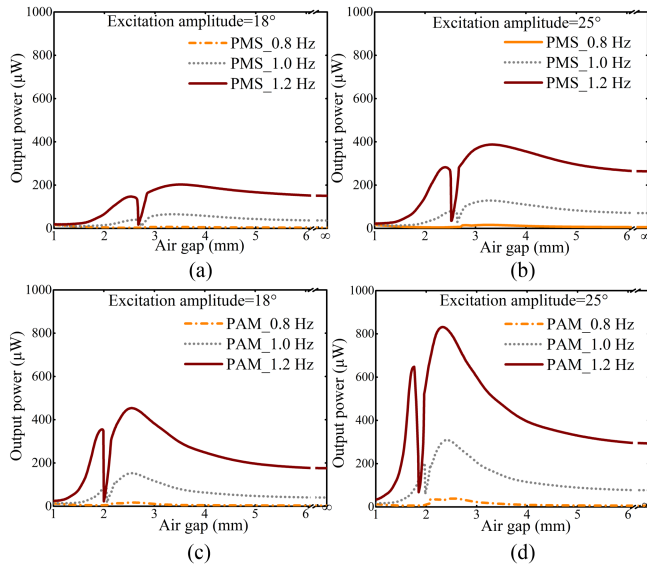* Unless specified, the values are applicable for all the configurations.

Fig. 7. Average output power of PMS and PAM with respect to the air gap of the magnetic spring under various excitation frequencies and amplitudes. (a) Excitation amplitude of 18° for PMS. (b) Excitation amplitude of 25° for PMS. (c) Excitation amplitude of 18° for PAM. (d) Excitation amplitude of 25° for PAM. The power of PMS and PAM at an infinite air gap corresponds to PLG and PAC, respectively. β and γ are zero.

Fig. 8. Fabricated prototype. (a) Photo of the prototype. (b) Components of the prototype.

where the proof mass is trapped at the equilibrium points created by gravity and strong magnetic force. With a further decreased air gap, the proof mass is held vertically by the magnetic spring since strong magnetic torque stabilizes the points around $\theta_r = \pm 180°$. In this case, the power output first rapidly increases from the valley point and reaches another peak, then begins to decrease. Tak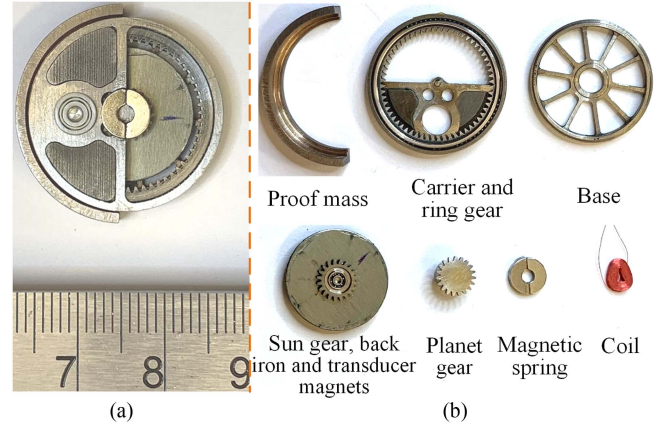ing the valley point as the critical point, the output power of the energy harvester undergoes an approximate mirror process with respect to the air gap because the stable equilibrium point of the energy harvester is reversed by the magnetic spring. From Fig. 8, compared with the configurations without magnetic spring (the output power at infinite air gap of PMS and PAM corresponds to the power of PLG and PAC, respectively), the magnetic spring could significantly enhance the output power if the air gap is properly selected. In addition, it seems that PMS could more effectively boost power generation than PAC for a certain range of air gaps. Compared with PMS, PAM achieves a more significant improvement in output power under the same excitation, which highlights the predominance of hybridizing all the power enhancement mechanisms. For given excitation amplitude and frequency, there exists an optimal air gap to achieve maximum power output. It seems that the optimal air gap shifts to a smaller value if the excitation amplitude becomes larger. In addition, the optimal air gap of PAM is larger than that of PAC in the same condition. The average kinetic energy may account for this. For more energetic excitation and larger eccentric mass, the energy harvester acquires higher kinetic energy such that stronger magnetic torque is required to trap the motion. Based on the simulation results, it is suitable to select an air gap that should not be smaller than the optimal value. Otherwise, the power may plunge into the valley because of manufacturing error. It is worth noticing that if the device orientation is changed, i.e., there exists a non-zero angle between the gravity vector and the axis y_0, the equivalent gravity potential energy well depth would become lower. This would cause a similar effect of the repulsive magnetic spring, and the curves shown in Fig. 7 shift to the right.

IV. EXPERIMENTAL VALIDATION

A. Prototype Fabrication

According to the design, a miniature prototype was fabricated to experimentally validate the hybrid power enhancement approach. As shown in Fig. 8, the dimension of the prototype is 25 mm × 4 mm (diameter × thickness, exclusive of magnetic spring). The total volume including the magnetic spring is

This article has been accepted for inclusion in a future issue of this journal. Content is final as presented, with the exception of pagination.

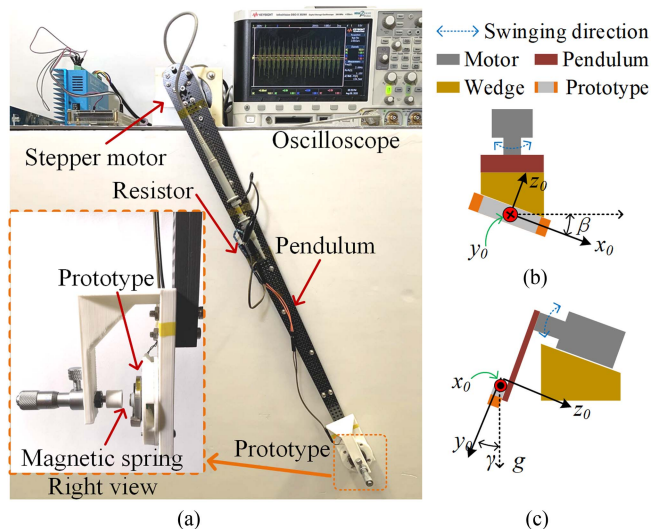CAI AND LIAO: TOWARD HIGH-PERFORMANCE WRIST-WORN ENERGY HARVESTER VIA HYBRID APPROACH

9

Fig. 9. Experimental setup. (a) Overview of the experimental setup. (b) Schematic illustration for configuring β. The wedge is fixed at the end of the pendulum and swings with the pendulum. (c) Schematic illustration for configuring γ. The motor is installed on the wedge.

2.01 cm^3. To the best of our knowledge, it is the smallest device among the wrist-worn energy harvesters. The total weight of the prototype (three power enhancement mechanisms are available) is 9.8 g. For convenient testing and simulation, one pair of the magnetic spring's magnets is permanently fixed on the carrier and the other pair can be easily removed when the magnetic spring is disabled. Furthermore, to configure the carrier to the asymmetric structure quickly, the filled space and the excavated space shown in Fig. 2(a) are designed as a component that can be easily disassembled.

B. Bench-Top Excitation Testing

To simulate the excitation of the human arm swing, an experimental setup shown in Fig. 9(a) was built. Although the energy harvester is designed for capturing the kinetic energy of human arm swinging motion, the motion simulator can generate more consistent excitations than a human being does. It can reduce the disturbances of inconsistent excitations and it is convenient to make performance comparisons between different configurations. Since the human arm swing resembles sinusoidal motion [27], a pendulum with a length of 50 cm was employed to mimic the human arm, which was driven by a stepper motor (Telesky HBS86H, China). The excitation frequencies and amplitude of the created sinusoidal motion ranged from 0.8–1.2 Hz and 18°–25°, respectively. The prototype was secured at the terminal of the pendulum and excited by the pendulum. A pair of the magnetic spring's magnets were fixed on a screw gauge (Mitutoyo IM 175, Japan) for quick setup and adjusting the air gap of the magnetic spring (see the right view of Fig. 9). To measure the output power, an optimal resistor was directly connected to the prototype without current rectification and its voltage was recorded by the oscilloscope (Keysight DSO-X 3024A, USA) to calculate the average power. In a real application, the current rectification should result in energy loss and thus the measurement without rectification will overestimate the output power. However, due to the ultralow voltage drop (as low as 43 mV for MAX40200, Analog Devices) of the commercial diodes, it is informative to evaluate the output power without rectification. For each trial, the experiments lasted for 60 s and were repeated 5 times with the same prototype. Then the average power was obtained by averaging the repeated data and standard deviations were calculated for the error bars of each trial. To evaluate the performance of different orientations of the device, a wedge was used to configure the angles of β and γ, as shown in Fig. 9(b) and (c).

Apart from measuring the average power, the combined damping coefficient was acquired to perform the simulations via a free oscillation experiment [18]. To this end, the base of the prototype was vertically fixed, and an optimal resistor was also used to dissipate the generated electricity. In the experiment, the proof mass was released to freely oscillate with an initial condition of $\theta_r = 90°$ and zero speed. A camera was employed to track the trajectory of the proof mass, which was used to obtain the combined damping coefficient via curve fitting. This process was repeated 5 times for different configurations of the prototype. Using this method, the combined damping coefficient b was measured to be 3.1×10^{-6} N·m·s/rad for CON, 3.05×10^{-5} N·m·s/rad for PLG and PMS, and 3.12×10^{-5} N·m·s/rad for PAC and PAM, respectively. By disconnecting the load resistor, the mechanical damping coefficient b_m for PLG, PMS, PAC, and PAM was measured to be 2.9×10^{-6} N·m·s/rad. Therefore, it leads to a transmission efficiency of $\eta_m = (1 - b_m/b) \times 100\% = (1 - 0.29/3.05 \sim 3.12) \times 100\% \approx 93.5\%$. With the efficiency of copper loss for $R_i = R_L$, the electrical efficiency $\eta_e = R_L/(R_i + R_L) \times 100\% = 50\%$. Then the total efficiency of PLG, PMS, PAC, and PAM is estimated to be $\eta = \eta_m \times \eta_e = 93.5\% \times 50\% = 46.75\%$.

C. Results and Discussions

As discussed, the optimal air gap of the magnetic spring depends on the excitation amplitudes and frequencies. However, the optimal air gap for a specific excitation amplitude and prototype configuration may lead to power deterioration of another excitation condition or configuration. To ensure the effectiveness of the magnetic spring for all the testing conditions and configurations, it seems to be safe to select an air gap that is not smaller than 3.5 mm from Fig. 7(a). In the experiment, we tentatively used different air gaps for PMS and PAM to experimentally determine the air gap of the magnetic spring under different excitation intensities (or excitation accelerations). The excitation acceleration is proportional to the square of the excitation frequency, excitation amplitude, or the pendulum length. Therefore, the average output power versus excitation frequency for different excitation amplitudes and configurations is presented, as shown in Fig. 10. It is observed that the value of maximum output power lies at 4.0 mm, instead of a smaller value that is predicted by the analytical model. This probably results from manufacture and assembling errors of the magnetic spring,
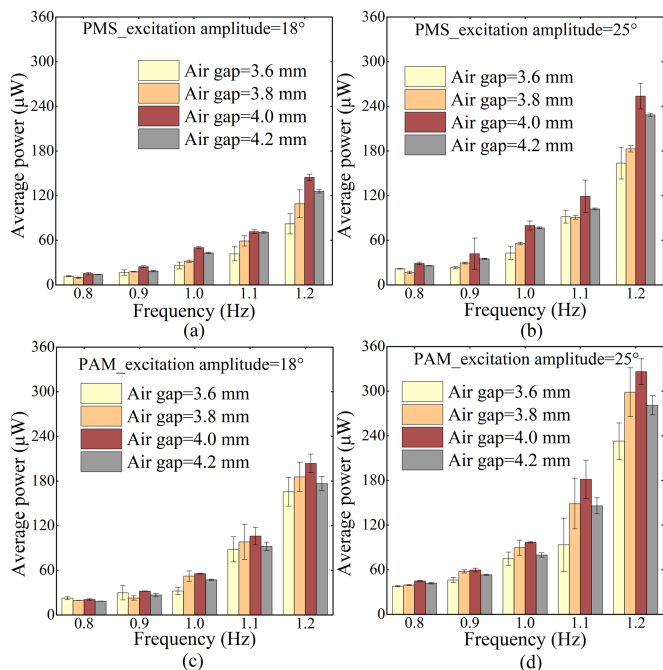
This article has been accepted for inclusion in a future issue of this journal. Content is final as presented, with the exception of pagination.

10   IEEE/ASME TRANSACTIONS ON MECHATRONICS

Fig. 10. Measured average output power of PMS and PAM for various air gaps of magnetic spring with zero β and γ. (a) Excitation amplitude of 18° for PMS. (b) Excitation amplitude of 25° for PMS. (c) Excitation amplitude of 18° for PAM. (d) Excitation amplitude of 25° for PAM.
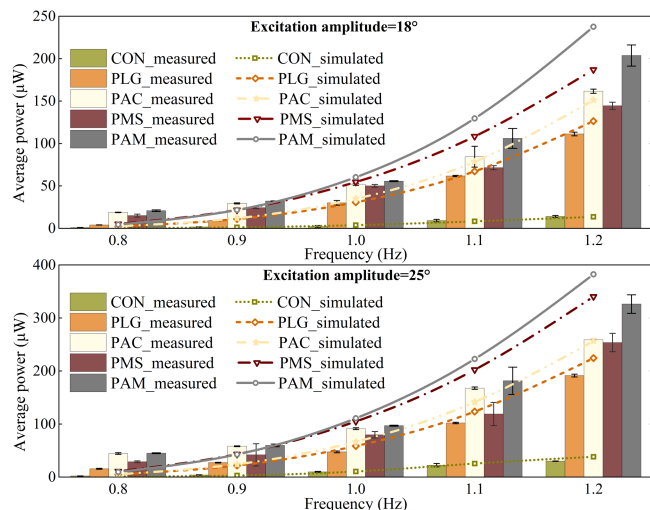

Fig. 11. Measured and simulated average output power with respect to excitation frequency for various configurations. The air gap of the magnetic spring is 4.0 mm for PMS and PAM. The angles of β and γ are zero.

which leads to asymmetric magnetic field distribution and creates an additional stable equilibrium point to trap the proof mass. The magnetic field asymmetry becomes more severe if the air gap is smaller. As a result, we found that the proof mass could be occasionally trapped and thus the output power is significantly weakened if the air gap is smaller than 4.0 mm. In addition, the asymmetric magnetic field exerts additional magnetic torque on the magnets of the transducers to constrain their motion. Such additional magnetic torque is then amplified by the planetary gear system and further reduces the output power. Apart from this, it is noted that the air gap of 3.8 mm for PAM outperforms the air gap of 4.2 mm in general while the results are contrary for PMS. Since PAM has the asymmetric carrier design, it seems that the effect of manufacture and assembling errors can be abated by increased eccentric mass. The prediction may be more accurate if the magnetic field asymmetry is considered in the model. However, the model will become extremely complicated, and the computing resource requirement may be unacceptably high. Moreover, it is difficult to precisely measure the magnetic field asymmetry effect because of the prototype's highly compact structure.

After determining the air gap of the magnetic spring, the average output power of different configurations for various excitation amplitudes and frequencies was also measured, as shown in Fig. 11. It can be observed that, within the testing frequency range, the output power is positively correlated with excitation intensity and the maximum power is achieved at 1.2 Hz for each configuration. It is worth noticing that the upper limit of output power may not exist since the potential energy curve of this energy harvesting system is periodic, and there exists the maximum potential energy point. Therefore, if the proof mass is energetic enough to overcome the maximum potential energy point, the output power could continue to increase with the excitation frequency. Using the measured data in Fig. 11, the power improvement range for the testing excitation frequencies and amplitude can be calculated. Compared with CON, PLG can improve the output power by 335%–1422% since the energy conversion capacity is significantly enhanced by the planetary gear system. Since PAC and PMS integrate one more power enhancement technique, the output power of these two configurations generally outperforms that of PLG, which further improves the output power by 35%–373% and 16%–278%, respectively. Although PAC and PMS are both equipped with two kinds of power enhancement mechanisms, it is observed that the output power of PAC is evidently higher than that of PMS. However, this result conflicts with the simulated power shown in Fig. 11, which is probably caused by the manufacturing and assembling errors that we have discussed. For PAM configuration, the prototype hybridizes three power enhancement mechanisms and has the best performance in average output power, which further improves the power of PAC and PAM by up to 26% and 56%, respectively. The power performance of different configurations can also be verified by the load voltage shown in Fig. 12. It shows that the configurations with the power enhancement approaches obtain remarkably higher voltage than that of CON, and PAM achieves the highest output voltage. This reveals that different power enhancement mechanisms integrated into the energy harvester can work together to maximize power improvement for the whole excitation range. With the air gap of 4.0 mm, PAM achieves a maximum power of 326.27±17.46 μW at 1.2 Hz for the excitation frequency of 25°. Besides, it is worth mentioning that compared with CON, PLG increases the volume by around 50% while the other configurations only require minimal additional space (less than 2.5% of PLG's volume). Therefore, with an extra volume of
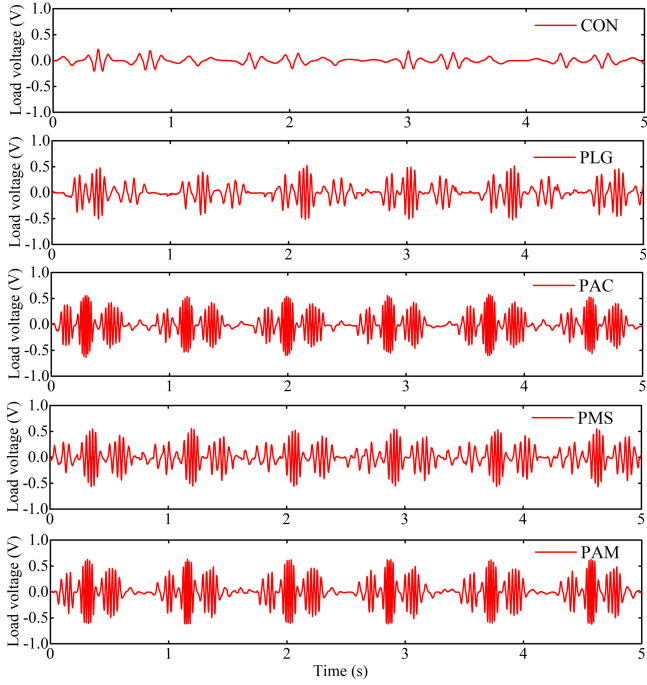
Fig. 12. Load voltage of different configurations at the excitation frequency of 1.2 Hz for the excitation amplitude of 25°.
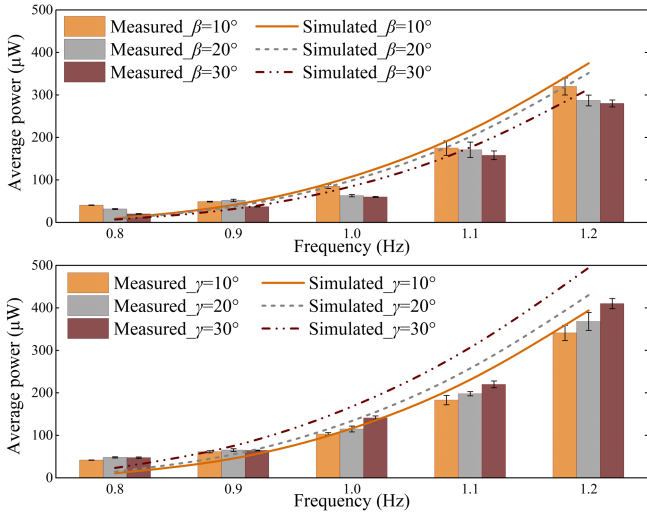

Fig. 13. Output power of PAM for different values of β and γ. The excitation amplitude is 25°.

TABLE IV
PERFORMANCE COMPARISON AMONG DIFFERENT DEVICES

Authors	Power (mW)	Volume (cm^3)	Power density (μW/cm^3)	Adopted approach*
This work	0.326	2.01	162.19	A+B+C
Maharjan et al. [14]	0.094	15.9	5.92	A
Cai and Liao [15]	1.46	3.21	454.82	A
Halim et al. [17]	0.061	20.1	3.03	B
Seiko AGS [21]	0.050	3.50	14.29	C
Kinetron MGS [22]	0.097	2.35	42.13	C
Cai and Liao [23]	1.74	5.03	345.92	C

* Adopted approach: (A) Enhanced motion capture capacity; (B) Enhanced displacement and velocity responses; (C) Improved energy conversion capacity.

thus the power decreases as β increases. On the other hand, an increasing γ serves to lower the gravity potential energy well depth. This effect is similar to the effect of the magnetic spring.

From Figs. 11 and 13, the simulation generally underestimates the output power for low frequencies. These differences between the simulation and the measurement may be caused by the additional vibration of the stepper motor. At a low speed, the motion of the stepper motor is usually unsmooth, and thus the excitation becomes more energetic. With increasing excitation frequency, this effect is attenuated since the stepper motor can generate smoother motion. However, at high excitation frequencies, the full-type groove element bearing that is equipped in the prototype undergoes kickback friction, which leads to overall overestimation in the simulation. Furthermore, the overestimation of the simulations for PMS and PAM is relatively large due to manufacturing and assembling errors of the magnetic spring. Besides these, it is interesting that the simulated power of PMS is slightly higher than that of PAM at low excitation frequencies. Two reasons may account for this result. First, the measured damping coefficient of PAM is slightly larger, and thus the captured motion is more easily damped. Second, since the eccentric mass of PAM is increased by asymmetric carrier design, it may require stronger magnetic torque to sufficiently lower the potential energy well depth to overperform PMS at low frequencies. Nonetheless, with increasing excitation frequency, PAM can gain a more significant advantage in output power.

Despite the discrepancies, the overall simulations match the measurement for other configurations, which validates the system dynamics model. Thus, the developed model seems to be sufficient for predicting the performance of the energy harvester on an average power basis, especially if more precise manufacturing and assembling technology is employed.

As given in Table IV, with the smallest volume among the counterparts, the proposed energy harvester performs much better than most of the existing devices in terms of output power and power density. Such improvement is contributed by the hybrid approach that enables the synergy effect of different mechanisms. Although the power density of our device is not the highest, it could be significantly increased based on the scaling law. Moreover, future optimization can also contribute to the improvement in power density.

around 54%, the hybridized power enhancement approach of PAM boosts the output power to 8–28 times that of CON. This highlights the preponderance of the hybrid power enhancement approach for wrist-worn energy harvester.

The average power of PAM for different β and γ is shown in Fig. 13. It is shown by both the simulation and experiments that with increasing β or decreasing γ, the output power decreases. For $\beta \neq 0$, the arm swinging motion does not coincide with the sagittal plane $O_0 x_0 y_0$, which leads to less intense excitation and

V. CONCLUSION AND OUTLOOKS

In this article, a wrist-worn energy harvester with the hybrid power enhancement approach was proposed to boost the performance of power generation. Based on a highly compact framework, the energy harvester integrated multiple approaches. A planetary gear system was employed to increase the energy conversion capacity and the asymmetric carrier of the planetary gear system was utilized to improve the motion capture capacity. In addition, a tiny repulsive magnetic spring was used to enhance displacement and velocity responses. To predict the performance of different power enhancement mechanisms, an analytical model was constructed. With the analytical model, the effects of different power enhancement mechanisms were theoretically analyzed, which revealed that the asymmetric carrier could effectively improve motion capture capacity and there existed an optimal air gap for the magnetic spring. A miniature prototype with a total volume of 2.01 cm^3 was fabricated to experimentally verify the proposed concept under bench-top excitations. Due to manufacturing and assembling errors, the air gap value of maximum power output lay at 4.0 mm while a smaller value was estimated by the simulation. In addition, the output power of various configurations was measured to quantify the power improvement of different power enhancement mechanisms. The results showed that compared with the conventional structure, the planetary gear system improved the output power by 335%–1422% at the price of increasing the total device volume by around 50%. With minimal additional device volume, the asymmetric carrier and magnetic spring further increased the power by 35%–373% and 16%–278%, respectively. By hybridizing all three approaches, the output power was finally boosted to 8∼28 times that of the conventional structure, achieving a maximum power of 326.27±17.46 μW. Thanks to significant improvement in output power, the hybrid approach provides a highly compact structure for a high-performance wrist-worn energy harvester. With a small size and high power output, the proposed energy harvester can be easily embedded in a smart watch to power several sensors, such as the pedometer and temperature sensors.

We recognize that there is much room to improve performance based on the above results and discussions. In the future, tailored magnetic shielding methods should be developed to reduce MI because of its negative effects on performance. Furthermore, a systematic optimization can be performed to further improve the output power. Finally, it will provide more insights to investigate the power generation performance under nonperiodic excitations.
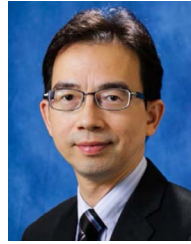
REFERENCES

[1] Z. Yang, S. Zhou, J. Zu, and D. Inman, "High-performance piezoelectric energy harvesters and their applications," *Joule*, vol. 2, no. 4, pp. 642–697, Apr. 2018.

[2] X. Wu, W. Cao, H. Yu, Z. Zhang, Y. Leng, and M. Zhang, "Generating electricity during locomotion modes dominated by negative work via a knee energy harvesting exoskeleton," *IEEE/ASME Trans. Mechatron.*, vol. 27, no. 6, pp. 4451–4461, Dec. 2022.

[3] T. S. Todorov, A. S. Fursov, R. P. Mitrev, V. V. Fomichev, S. S. Valtchev, and A. V. ll'in, "Energy harvesting with thermally induced vibrations in shape memory alloys by a constant temperature heater," *IEEE/ASME Trans. Mechatron.*, vol. 27, no. 1, pp. 475–484, Feb. 2022.

[4] N. A. Hossain, G. G. Yamomo, R. Willing, and S. Towfighian, "Characterization of a packaged triboelectric harvester under simulated gait loading for total knee replacement," *IEEE/ASME Trans. Mechatron.*, vol. 26, no. 6, pp. 2967–2976, Dec. 2021.

[5] S. Gao et al., "A lightweight wireless overpressure node based efficient monitoring for shock waves," *IEEE/ASME Trans. Mechatron.*, vol. 26, no. 1, pp. 448–457, Feb. 2021.

[6] Y. Gao, J. Liang, and Y. Liao, "Multiple harmonics extended impedance model of piezoelectric energy harvesting systems," *IEEE/ASME Trans. Mechatron.*, vol. 27, no. 7, pp. 1185–1195, Apr. 2022.

[7] C.-L. Yang, K.-W. Chen, and C.-D. Chen, "Model and characterization of a press-button-type piezoelectric energy harvester," *IEEE/ASME Trans. Mechatron.*, vol. 24, no. 1, pp. 132–143, Feb. 2019.

[8] M. Liu, C. Hill, R. Queen, and L. Zuo, "A lightweight wearable biomechanical energy harvester," *Smart Mater. Struct.*, vol. 30, no. 7, Jan. 2021, Art. no. 075032.

[9] B. Wang, Z. Long, Y. Hong, Q. Pan, W. Lin, and Z. Yang, "Woodpecker-mimic two-layer band energy harvester with a piezoelectric array for powering wrist-worn wearables," *Nano Energy*, vol. 89, Nov. 2021, Art. no. 106385.

[10] H. Fu et al., "Rotational energy harvesting for self-powered sensing," *Joule*, vol. 5, no. 5, pp. 1074–1118, May 2021.

[11] R. Rantz and S. Roundy, "Dynamics of wrist-worn eccentric-rotor energy harvesters," *Phys. Rev. Appl.*, vol. 14, no. 1, Jul. 2020, Art. no. 014058.

[12] M. Li, H. Deng, Y. Zhang, K. Li, S. Huang, and X. Liu, "Ultra-low frequency eccentric pendulum-based electromagnetic vibrational energy harvester," *Micromachines*, vol. 11, no. 11, Nov. 2020, Art. no. 1009.

[13] H. Liu et al., "A non-resonant rotational electromagnetic energy harvester for low-frequency and irregular human motion," *Appl. Phys. Lett.*, vol. 113, Nov. 2018, Art. no. 203901.

[14] P. Maharjan, R. M. Toyabur, and J. Y. Park, "A human locomotion inspired hybrid nanogenerator for wrist-wearable electronic device and sensor applications," *Nano Energy*, vol. 46, pp. 383–395, Apr. 2018.

[15] M. Cai and W. H. Liao, "High power density inertial energy harvester without additional proof mass for wearables," *IEEE Internet Things J.*, vol. 8, no. 1, pp. 297–308, Jan. 2021.

[16] C. Li, S. Wu, P. C. K. Luk, M. Gu, and Z. Jiao, "Enhanced bandwidth nonlinear resonance electromagnetic human motion energy harvester using magnetic springs and ferrofluid," *IEEE/ASME Trans. Mechatron.*, vol. 24, no. 2, pp. 710–717, Apr. 2019.

[17] M. A. Halim, R. Rantz, Q. Zhang, L. Gu, K. Yang, and S. Roundy, "An electromagnetic rotational energy harvester using sprung eccentric rotor, driven by pseudo-walking motion," *Appl. Energy*, vol. 217, pp. 66–74, May 2018.

[18] M. Cai and W. H. Liao, "Enhanced electromagnetic wrist-worn energy harvester using repulsive magnetic spring," *Mech. Syst. Signal Process.*, vol. 150, Mar. 2021, Art. no. 107251.

[19] R. Lockhart, P. Janphuang, D. Briand, and N. F. de Rooij, "A wearable system of micromachined piezoelectric cantilevers coupled to a rotational oscillating mass for on-body energy harvesting," in *Proc. IEEE 27th Int. Conf. Micro Electro Mech. Syst.*, 2014, pp. 370–373.

[20] P. Pillatsch, E. M. Yeatman, and A. S. Holmes, "A piezoelectric frequency up-converting energy harvester with rotating proof mass for human body applications," *Sensors Actuators A, Phys.*, vol. 206, pp. 178–185, Feb. 2014.

[21] T. Xue, S. Kakkar, Q. Lin, and S. Roundy, "Characterization of microgenerators embedded in commercial-off-the-shelf watches for wearable energy harvesting," *Proc. SPIE, Ind. Commercial Appl. Smart Struct. Technol.*, vol. 9801, 2016, Art. no. 98010O.

[22] T. Xue, S. Williams, R. Rantz, M. A. Halim, and S. Roundy, "System modeling, characterization, and design considerations for generators in commercial watches with application to energy harvesting for wearables," *IEEE/ASME Trans. Mechatron.*, vol. 23, no. 5, pp. 2515–2524, Oct. 2018.

[23] M. Cai, J. Wang, and W. H. Liao, "Self-powered smart watch and wristband enabled by embedded generator," *Appl. Energy*, vol. 263, Apr. 2020, Art. no. 114682.

[24] M. Cai and W. H. Liao, "Design, modeling and experiments of electromagnetic energy harvester embedded in smart watch and wristband as power source," *IEEE/ASME Trans. Mechatron.*, vol. 26, no. 4, pp. 2104–2114, Aug. 2021.

[25] N. Zhou, Y. Zhang, C. R. Bowen, and J. Cao, "A stacked electromagnetic energy harvester with frequency up-conversion for swing motion," *Appl. Phys. Lett.*, vol. 117, no. 16, Oct. 2020, Art. no. 163904.

[26] Z. Li, Z. Yan, J. Luo, and Z. Yang, "Performance comparison of electromagnetic energy harvesters based on magnet arrays of alternating polarity and configuration," *Energ. Convers. Manage.*, vol. 179, pp. 132–140, Jan. 2019.

[27] B. Hejrati, S. Chesebrough, K. B. Foreman, J. J. Abbott, and A. S. Merryweather, "Comprehensive quantitative investigation of arm swing during walking at various speed and surface slope conditions," *Hum. Movement Sci.*, vol. 49, pp. 104–115, Oct. 2016.

Wei-Hsin Liao (Senior Member, IEEE) received the Ph.D. degree in mechanical engineering from The Pennsylvania State University, University Park, PA, USA, in 1997.

He is Choh-Ming Li Professor of Mechanical and Automation Engineering, The Chinese University of Hong Kong, Hong Kong. His research interests include smart materials and structures, energy harvesting, vibration control, mechatronics, exoskeleton and prosthesis.

Dr. Liao is currently an Associate Editor for *Journal of Intelligent Material Systems and Structures*, and on the Executive Editorial Board of *Smart Materials and Structures*. He is a Fellow of the American Society of Mechanical Engineers, the Institute of Physics, and the Hong Kong Institution of Engineers.

Mingjing Cai (Member, IEEE) received the Ph.D. degree in mechanical and automation engineering from The Chinese University of Hong Kong, Hong Kong, in 2020.

He is currently an Associate Professor with Guangzhou Institute of Technology, Xidian University, Guangzhou, China. His current research interests include energy harvesting from human motion and self-powered IoT applications.